JOURNAL OF MATERIALS SCIENCE 30 (1995) 5415–5426

$MoSi_2$ diffusion barrier for the passivation of copper at elevated temperatures

R. CVITKOVIC, D.G. IVEY
Department of Mining, Metallurgical and Petroleum Engineering, University of Alberta, Edmonton, Alberta, Canada T6G2G6

J. STILES
Sherrit Inc., Fort Saskatchewan, Alberta, Canada T8L 2P2

Sputter deposited $MoSi_2$ coatings (200 and 400 nm thick) on copper have been studied in an attempt to prevent or at least reduce the oxidation of copper. Samples were exposed to an air ambient at temperatures ranging from 600–850 °C for up to 15 min. Sputter-deposited $MoSi_2$ was amorphous upon deposition and crystallized on annealing. Silicon from the $MoSi_2$ was found to diffuse into the copper causing the $MoSi_2$ to transform to lower silicides. The primary oxidation product for $MoSi_2$-coated samples was CuO (with small amounts of Cu_2O), which is in contrast to uncoated copper where Cu_2O is the main oxidation product. The amount of copper consumed by oxidation, for a 200 nm $MoSi_2$ barrier relative to uncoated copper, was reduced by $\approx$140 times at 600 °C and $\approx$30 times at 800 °C. A 400 nm $MoSi_2$ coating yielded an improvement of $\approx$420 times at 600 °C, and $\approx$200 times at 850 °C. For the 400 nm barrier exposed to air for 15 min, this corresponds to a 35 nm CuO layer at 600 °C and a 300 nm thick oxide layer at 850 °C.

1. Introduction

Copper is being considered as a low-cost electrical interconnect in VLSI (very large scale integrated) and thick-film technologies, because of its good electromigration resistance and conductivity. Unfortunately, copper oxidizes readily at the elevated temperatures utilized for processing.

Thick films are used as interconnects in hybrid microcircuits. Thick-film conductor pastes are traditionally made from precious metals such as gold, silver, palladium and platinum or some combination of these [1, 2]. The metals are in the form of inorganic powders in organic fluid vehicles, which are made into pastes and screen printed on to ceramic substrates, such as alumina. The pastes are dried, temporary binders are removed by oxidation in air, and then sintered at temperatures from 800–850 °C. The above-mentioned powders do not oxidize in air at the processing temperatures required; however, they are very expensive. There is an interest in developing non-noble metals as replacements, with copper being a prime candidate.

Copper is increasingly being touted as a metallization material for interconnects in VLSI circuits, because of its low bulk electrical resistivity (1.7 μΩ cm versus 2.7 μΩ cm for aluminium), good electromigration resistance and relatively low cost [3–5]. As dimensions of VLSI circuits are scaled down in order to increase circuit density, stability and performance, interconnects are becoming increasingly important, particularly for multilayered structures. There are advantages to using copper as an interconnect material, provided problems such as oxidation, diffusion in silicon, adhesion and patterning, can be addressed.

The prime objective of the present work was to investigate the performance of a diffusion barrier for copper, in an effort to prevent or at least minimize copper oxidation at elevated temperatures. Such a barrier could have potential application for copper interconnects in VLSI and thick-film applications. For a barrier to be successful, a number of criteria need to be satisfied. These are listed below, in no particular order.

1. Low diffusivity for oxygen and copper.
2. Immiscibility in copper and vice versa.
3. Good electrical conductivity.
4. Good adhesion with copper.
5. Inexpensive processing.
6. Resistance to oxidation.

Chemical compounds, such as transition metal nitrides, carbides, borides and silicides are potential barrier candidates because of their large negative heats of formation, high melting points and relatively low resistivities [6]. Silicides, in particular, were of interest here, in part because of the wealth of data available on oxidation behaviour. Oxidation studies have been done on transition metal silicides, i.e. $CoSi_2$ [7, 8], $NiSi_2$ [9] and PtSi [7], and refractory metal silicides, i.e. $TiSi_2$ [10], $HfSi_2$ [11], $TaSi_2$ [12], $MoSi_2$ [13, 14] and WSi_2 [15–17]. The silicon rich silicides are generally of most interest, as these are usually the most stable. Of these, refractory metal silicides are particularly attractive because they have higher melting points than transition metal silicides. Relevant properties for refractory silicides are listed in Table I.

0022–2461 © *1995 Chapman & Hall*

TABLE I Selected properties of refractory metal silicides and their oxides

	Melting point (°C) [18, 19]	Resistivity (μΩ cm) [19]	$-\Delta H_f$ (kJ/O atom) [19, 20]	$-\Delta H_f$ (kJ/metal atom) [19, 20]
$TiSi_2$	1540	13, 25		134
TiO_2			1925	917
$ZrSi_2$	1700	35–40		226
ZrO_2			2294	1097
$HfSi_2$	1800	45–50		226
HfO_2			2348	1122
VSi_2	1670	50–55		310
V_2O_5			1348	800
$NbSi_2$	1950	50		138
Nb_2O_5			1628	967
$TaSi_2$	2200	35–55		117
Ta_2O_5			1754	1047
$CrSi_2$	1550	≈ 600		121
CrO_3			787	573
$MoSi_2$	1980	21, 100		117
MoO_3			1051	753
WSi_2	2165	12, 70		92
WO_3			1155	841
Cu_2O			1155	85
CuO			720	157
SiO_2			666	

Of the silicides listed in Table I, $CrSi_2$ was discounted because of its high resistivity relative to the others. $TiSi_2$ and $ZrSi_2$ have low resistivities, but have fairly low melting points and zirconium and titanium form oxides with more negative heats of formation than SiO_2. $HfSi_2$ and WSi_2 are not good candidates, because hafnium oxide has the most negative heat of formation per oxygen atom of the refractory metals and WSi_2 pests at elevated temperatures. This leaves $NbSi_2$, $TaSi_2$ and $MoSi_2$ as the best candidates for diffusion barriers and from these $MoSi_2$ was selected for this particular study.

Bulk $MoSi_2$ has good high-temperature oxidation resistance (600–1800 °C), superior to virtually all other disilicides, which is due to the formation of a self-passivating SiO_2 surface layer [21]. The passivating layer deteriorates, however, at temperatures exceeding 1800 °C, when oxygen diffusion through SiO_2 drastically increases leading to the formation of volatile SiO. At low temperatures (375–500 °C), $MoSi_2$ is susceptible to pesting, which was first documented by Fitzer in 1955 [22]. Pesting is a process whereby volatile MoO_3 forms in addition to SiO_2 [23, 24], resulting in the development of substantial internal stresses and ultimately disintegration of the silicide. At 500–550 °C, there is a transition from pesting to selective oxidation of silicon to form SiO_2. Pesting was not anticipated to be a problem in this study, because the temperature range of interest was 600–850 °C.

$MoSi_2$ is one of three silicides in the Mo–Si system. The others are Mo_3Si and Mo_5Si_3. $MoSi_2$ exhibits a combination of ceramic and metallic properties, with mixed covalent/metallic bonding. $MoSi_2$ is polymorphic, although only one stable form (the α phase) exists at the temperatures of interest in this work (< 1000 °C). The α phase has a tetragonal tI6 structure with $a = 0.321$ nm and $c = 0.785$ nm [25]. In addition to stable crystalline forms, $MoSi_2$ can also exist as a metastable hexagonal form with $a = 0.4596$ nm and $c = 0.655$ nm [25]. The thermal expansion coefficient for α-$MoSi_2$ is $7–10 \times 10^{-6}$ °C^{-1} in the 20–1400 °C range and the thermal conductivity is 65 Wm^{-1} K^{-1} at room temperature and decreases to 30 Wm^{-1} K^{-1} at 1400 °C [26]. Mo_3Si has a cubic cP8 structure with $a = 0.489$ nm, while Mo_5Si_3 has a tetragonal structure with $a = 0.9648$ nm and $c = 0.4913$ nm [25].

2. Experimental procedure

Single-crystal ⟨1 0 0⟩ oriented silicon substrates were utilized for all oxidation experiments involving diffusion barriers. SiO_2 layers were grown on top of the wafers to isolate the silicon substrate from subsequent deposited metal and barrier layers, as copper dissolves ≈12 at % Si at 850 °C and forms several silicides with silicon. Oxide growth was done by either plasma-enhanced chemical vapour deposition (PE–CVD) or by wet oxidation. Prior to oxide growth, the silicon wafers were cleaned using a piranha etch of three parts by volume sulphuric acid and one part hydrogen peroxide. For PE–CVD, SiO_2 was grown on one side only, while for wet oxidation, SiO_2 was grown on both sides of the wafer. Wet oxidation was done by bubbling nitrogen, as the carrier gas, at 2 MPa through boiling water into the growth chamber. Oxidation was carried out for 2.5–3 h at 1100 °C. After oxidation, a copper layer followed by a $MoSi_2$ capping layer were deposited by magnetron sputtering. The deposition conditions for copper were 8 mtorr argon pressure, 20.5 standard cm^3 min^{-1} argon flow, 800 W power and a current of 1.71 A. The conditions for $MoSi_2$ deposition were 8 mtorr argon pressure, 20.5 standard cm^3 min^{-1} flow, 100 W argon power and a current of 1.14 A. A base pressure of 10^{-6} torr (1 torr = 133.322 Pa) was obtained before sputtering, and all samples were oscillated through 9° and rotated at a rate of 0.5 r.p.m. during deposition to improve film uniformity. Both copper and $MoSi_2$ were deposited in the same chamber without breaking vacuum. Copper layers, in all samples, were 2 μm thick, while $MoSi_2$ diffusion barriers were 100, 200 or 400 nm thick.

Oxidation experiments were also done on copper samples without $MoSi_2$ diffusion barriers. For these experiments, electrolytic tough pitch (ETP) copper, with less than 0.05% oxygen content, was utilized. Specimens were prepared by sectioning copper sheets (2 cm × 2 cm × 0.625 mm), then polishing with 400 and 600 grit SiC paper, followed by polishing with 6.0 μm diamond and 0.3 μm alumina. As a final step, copper samples were cleaned in a dilute nitric solution followed by rinsing in deionized water.

Samples were annealed in air in a Radiant Technology Corporation (RTC) infrared belt furnace Model Cu-900, which is the type of furnace commonly used for firing thick-film pastes. The furnace had four independently controllable heating zones with an air-cooling section directly following the last zone. Furnace belt speed was controlled to attain minimum ramp

times and appropriate peak times. Four temperatures, i.e. 600, 700, 800 and 850 °C, were used for times ranging from 2–15 min. Because annealing times were relatively short, kinetic calculations were done using annealing times corresponding to the peak temperature only and for times corresponding to $\geqslant 90\%$ of the peak temperature, to determine the effect of ramp time on the data obtained. The effect was minimal, i.e. the slopes of kinetic plots (oxide thickness versus the square root of time) varied by $\approx 5\%$; as a result, only data for peak temperatures are reported here.

A number of techniques were used to monitor oxide growth and microstructural changes. These include X-ray diffraction (XRD), light microscopy (LM), atomic force microscopy (AFM), scanning electron microscopy (SEM) and transmission electron microscopy (TEM). AFM was done primarily on as-deposited samples, to identify and quantify local roughness. Scans of 25 μm or less were done with a force of ≈ 0.1 nN and a scan rate of 6–10 Hz. Scanning electron (SEM) and light (LM) microscopy samples were examined in both plan-view and cross-section. Light microscopy was done using a Zeiss Ultraphot II LM, while SEM analysis was done in a Hitachi S-2700 SEM, equipped with a LinK eXL energy dispersive X-ray (EDX) analyser. Higher resolution imaging and microanalysis were done using a JEOL 2010 TEM, equipped with an ultrathin window, germanium X-ray detector or a Hitachi H-7000 TEM. Both cross-section and plan-view specimens were prepared using a combination of mechanical polishing and ion-milling methods. Oxide thicknesses were measured from either transmission or scanning electron micrographs.

3. Results and discussion

3.1. Oxidation of copper

Although kinetic data for the oxidation of copper were available in the literature, an oxidation study of copper, was completed using similar furnace profiles as the samples with diffusion barrier coatings. Thus, a direct comparison could be made between bare copper and the $MoSi_2$ barrier samples.

Both Cu_2O and CuO formed on the surface of copper with Cu_2O forming adjacent to metallic copper, i.e. $Cu/Cu_2O/CuO$. Fig. 1 shows a typical optical micrograph taken from an 800 °C anneal for a nominal time of 15 min. Cu_2O is the predominant oxidation product. The percentage of CuO, as a fraction of the total oxide thickness, varied from 5%–10% at 600 °C, 2%–5% at 700 °C, and 0%–2% above 800 °C. The dark gap between the copper and the Cu_2O is a sample preparation artefact, a result of delamination of the oxide layer from the copper substrate during sample preparation. The ratio of the linear coefficients of thermal expansion between copper and Cu_2O is 4.32, which is high enough for oxide separation to occur during cooling from elevated temperatures. The surface oxide was inspected by eye after annealing. It remained intact as a continuous planar sheet, for the 850 and 800 °C samples, but did not adhere to the surface of the metallic copper. The oxide for the 700 and 600 °C anneals, and particularly for the shorter

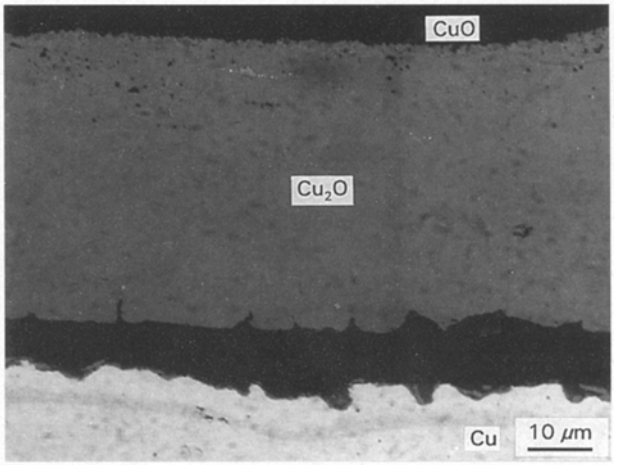

Figure 1 Optical micrograph of oxide growth on bare copper, annealed at 800 °C for 15 min. The outer CuO layer is barely visible.

annealing times, was flaky and non-uniform; however, there were areas where the oxide remained intact. These areas were subsequently used for oxide thickness measurements. The oxide at lower temperatures was thinner and structurally weaker than the oxides that formed at the higher temperatures, thus causing it to spall to a greater extent.

Thickness measurements were made on the oxide and comparisons were made with literature values. Fig. 2 and Table II summarize the results of the copper oxidation experiments. The oxide growth fits parabolic growth behaviour for bare copper at all temperatures studied (Fig. 2). A minimum of 50 measurements was taken for each data point, and the standard deviation for each point is less than the size of the data marker. Table II shows a comparison of literature values of parabolic rate constants with experimental rate constants. The literature values are given for the total oxide present. Because of the difficulty in measuring CuO thicknesses, experimental values are given for the Cu_2O only. These values should be conservative (for later comparisons) because they underestimate the total oxide thickness. The amount of copper consumed was also calculated from the experimental thickness data assuming a compact and planar Cu_2O oxide and again these are conservative values. These data will be used in later sections to evaluate the effectiveness of the $MoSi_2$ diffusion barriers. Fig. 3 shows an Arrhenius plot of the data in Fig. 2. The apparent activation energy is $Q_{app} = 83.6\ kJ\ mol^{-1}$.

Previous studies on copper oxidation show good agreement among different investigators at high temperatures, but this agreement becomes progressively poorer as the temperature decreases. Thick oxide scales on copper are composed of an inner layer of Cu_2O and an outer one of CuO, which is in agreement with the theory of composite oxide layers developed by Wagner [29, 30] and Valensi [31]. At temperatures greater than 800 °C, CuO is prone to porosity and is not considered to contribute to the growth rate of the oxide scale. Below 800 °C, the CuO content of the scale increases with decreasing temperature. However, empirical data collected by various authors for the

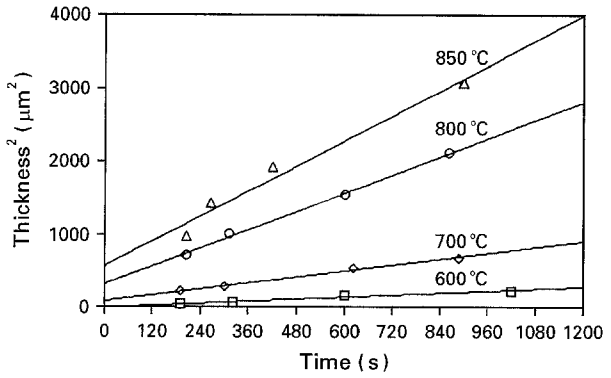

Figure 2 Plots of thickness squared versus time for the oxidation of bare copper for 600, 700, 800, and 850 °C.

TABLE II Comparison of parabolic rate constants for bare copper

T (°C)	k_p 10^{-8} [27, 28]	$cm^2 s^{-1}$ present work	Oxide thickness at 15 min (μm)	Copper consumed at 15 min (μm)
850	2.86–2.82	2.85	56.0	33.9
800	0.733–1.175	2.10	46.9	28.4
700	0.123–0.316	0.692	26.5	16.1
600	0.0153–0.145	0.230	14.1	8.54

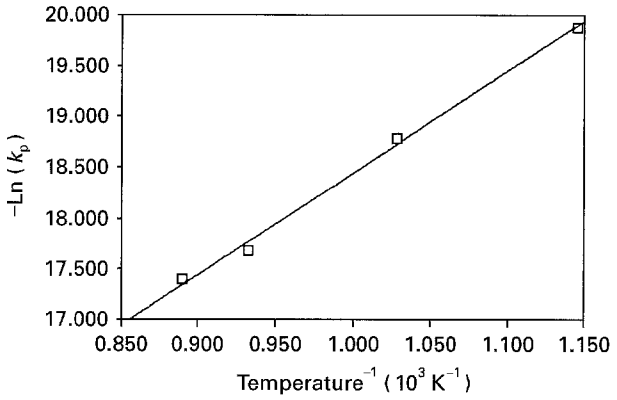

Figure 3 Arrhenius plot of the experimental rate constants. The slope is proportional to the effective activation energy of copper oxidation. $Q_{app} = 83.6\ kJ\ mol^{-1}$.

percentage of CuO varies. There is progressively increasing disagreement regarding relative ratios of Cu_2O and CuO below 800 °C. The percentage of CuO ranges from 0%–15% at 800 °C, from 5%–30% at 700 °C and 15%–55% at 600 °C [32]. Below ≈250 °C, Cu_2O is the only oxide formed during the earlier stages of the reaction, and even when CuO does eventually appear, it does not become predominant [32].

Our results show qualitative agreement with previous work reported in the literature; however, the percentage of CuO in all cases is lower for our work. CuO may have spalled from the surface of Cu_2O (particularly at lower annealing temperatures), leaving behind a thin residual layer, because the actual thickness of CuO did not change appreciably with temperature. Another possible explanation for a thinner CuO layer may be related to the short oxidation times in this study. In previous work, the composition of the oxide layer was found to be a function of time during the earlier stages of reaction, but it appeared to become constant with prolonged oxidation [33–36].

From Table II it is evident that the experimental rate constant values are higher for this work compared with the data taken from the literature in all cases, but are in close agreement at 800 and 850 °C. This may be related to the relatively short annealing times used in this work and the effect of ramping during both heating and cooling. The barrier samples, discussed in subsequent sections, have been annealed under the same conditions as the bare copper. Also, because the thickness measurements have been made on Cu_2O oxide only, they are conservative. A direct comparison between the bare copper samples and diffusion barrier samples will be made in later sections.

3.2. Oxidation of copper with a $MoSi_2$ diffusion barrier

Three different $MoSi_2$ barrier thicknesses were deposited, i.e. 100, 200 and 400 nm thicknesses. Prior to oxidation experiments, all as-deposited samples were

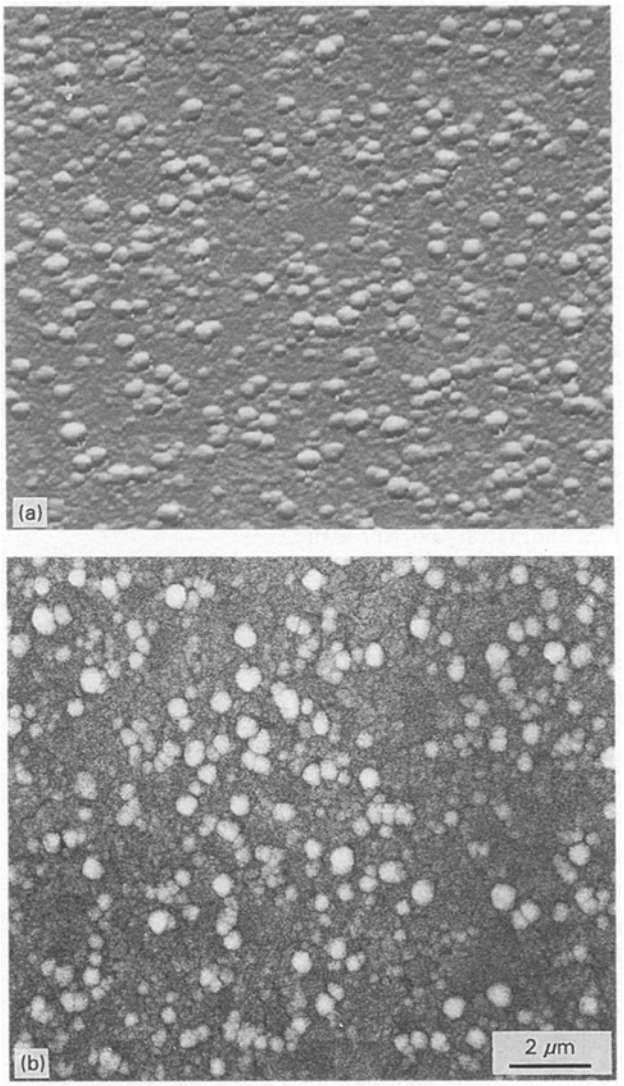

Figure 4 (a) AFM image and (b) SEM SE image of the top surface of a copper layer coated with a 400 nm $MoSi_2$ diffusion barrier. Both samples are imaged prior to annealing.

examined in the SEM and AFM. There was good correlation between the AFM images and the SEM images, as is evident in the micrographs from the 400 nm barrier sample (Fig. 4). In both types of image, agglomeration of the amorphous $MoSi_2$ layer is apparent. Surface roughness was quantifiable in the AFM, through the use of line scans – effectively using the AFM as a very sensitive profilometer. Surface roughness for all barrier thicknesses was similar, with average roughness, R_a, values less than 30 nm and maximum roughness values as large as ≈ 100 nm. For the 100 nm barriers, holes (1–3 μm^2 in size) were frequently observed in the as-deposited samples. These were believed to penetrate to the underlying copper (or at least very close to the copper), rendering the barrier ineffective in those areas. Consequently, oxidation tests were only done on the 200 nm and 400 nm barrier samples.

TEM bright-field imaging of as-deposited samples showed that the $MoSi_2$ barrier layer was continuous and close to its nominal thickness of 200 or 400 nm. For both layer thicknesses, the as-deposited $MoSi_2$ was amorphous.

The oxide growth behaviour, for the 200 nm barrier samples, is demonstrated in a series of SEM secondary electron (SE) images for 10 min anneals at 600, 700, 800 and 850 °C (Fig. 5). At 600 °C (Fig. 5a), only a thin oxide layer has formed (detected by EDX analysis), as the underlying $MoSi_2$ is still visible. At 700 °C (Fig. 5b), the oxide is thicker, producing a three-dimensional network on top of $MoSi_2$. The oxide layer becomes more dense at higher temperatures, eventually forming a coating with a grain size of ≈ 3–5μm (Fig. 5d). Oxide growth kinetics will be discussed later; however, it is noteworthy that at 600 °C and 10 min, 2 μm of bare copper (the thickness of the layer used for the barrier samples) would have completely oxidized to form a copper oxide duplex layer (Cu_2O and CuO).

Significant improvement in oxidation resistance was achieved by doubling the barrier thickness. SEM SE images, comparing 200 nm $MoSi_2$ and 400 nm $MoSi_2$ barrier samples, at 600 °C for 10 min and 850 °C for 10 min, are shown in Fig. 6. For samples annealed at 600 °C there is not much difference in surface morphology between the two because the oxide is very thin in both cases (80 nm for the 200 nm $MoSi_2$ barrier and < 10 nm for the 400 nm $MoSi_2$ barrier). The underlying $MoSi_2$ is visible for both samples. There is, however, a significant difference for

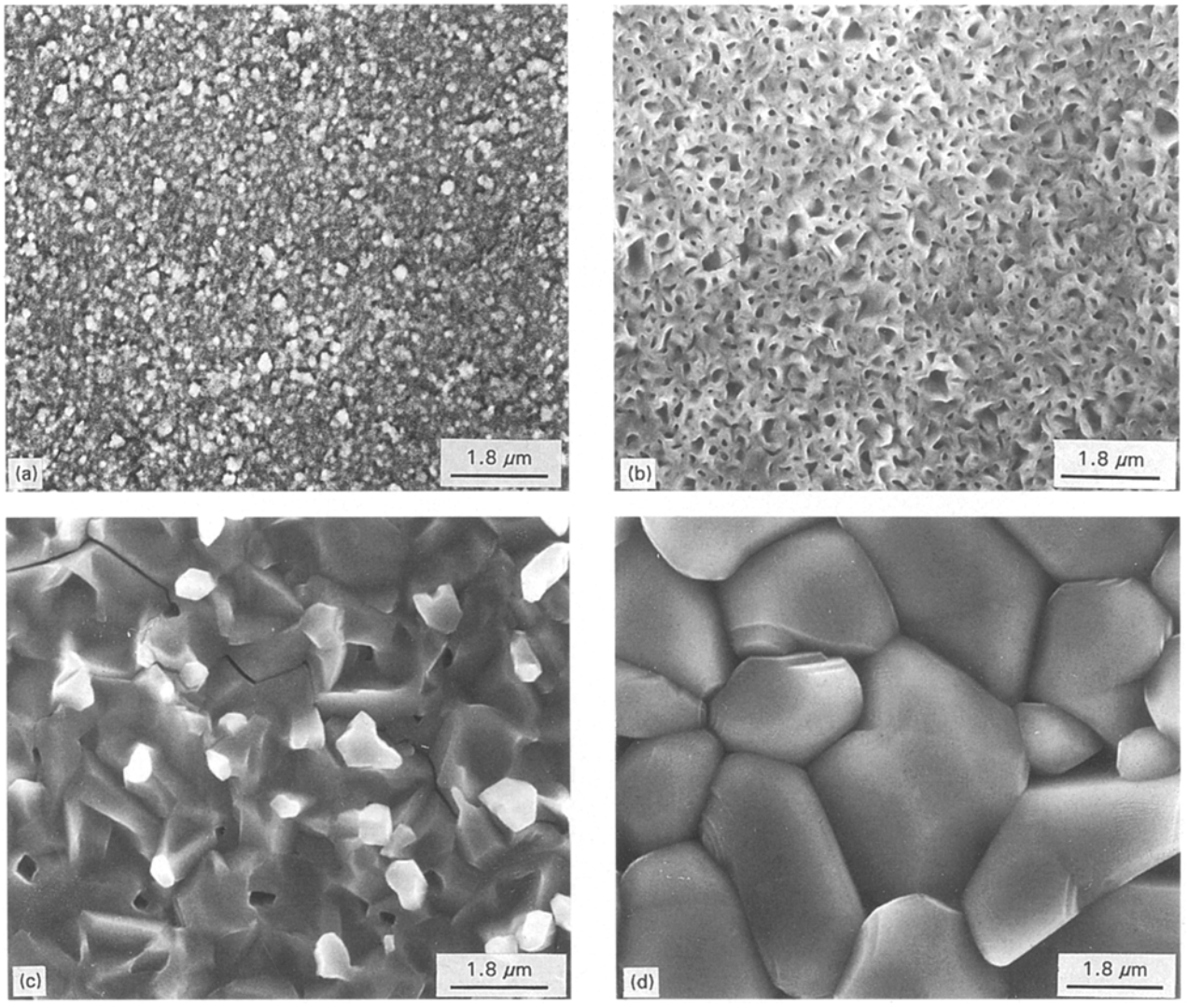

Figure 5 SEM SE images of 200 nm barrier samples annealed at (a) 600 °C for 10 min, (b) 700 °C for 10 min, (c) 800 °C for 10 min, and (d) 850 °C for 10 min.

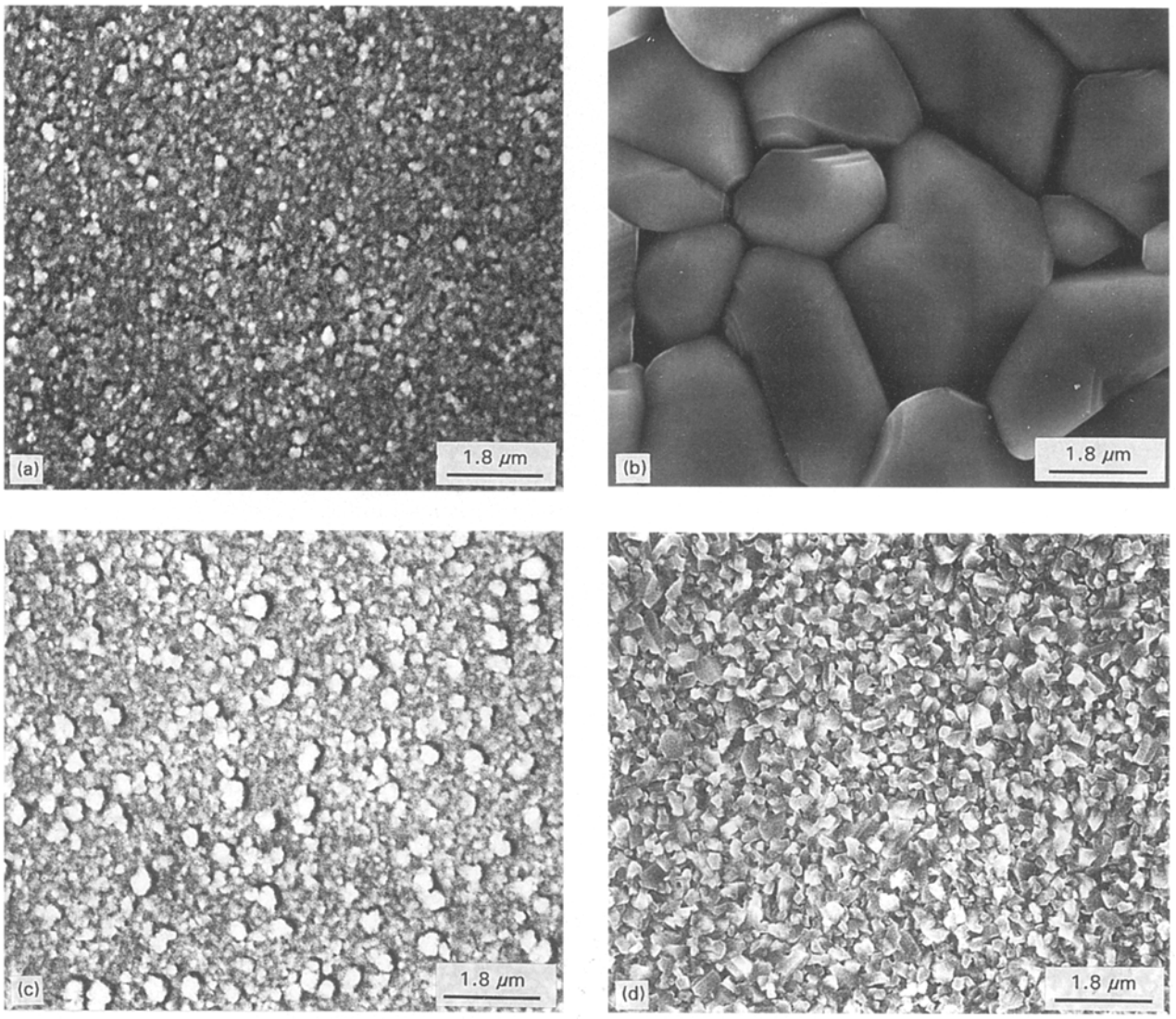

Figure 6 SEM SE images of 200 nm barrier samples annealed at (a) 600 °C for 10 min and (b) 850 °C for 10 min, and 400 nm barrier samples annealed at (c) 600 °C for 10 min and (d) 850 °C for 10 min.

the samples annealed at 850 °C. The oxide on the 200 nm barrier is ≈3.7 μm thick with a grain size of ≈3–5 μm, whereas the oxide is only ≈230 nm thick for the 400 nm barrier.

Fig. 7 shows representative XRD spectra for as-deposited samples and samples annealed at 800 °C for 15 min with 200 and 400 nm $MoSi_2$ barriers. The as-deposited spectrum shows only peaks corresponding to copper. There were no peaks for the $MoSi_2$ layer (which is expected because it is amorphous) or the underlying silicon substrate (the 4 0 0 peak for silicon shows up in some of the annealed samples). There is also a slight ⟨1 1 1⟩ preferred orientation in the direction perpendicular to the substrate for as-deposited copper. Annealed samples show evidence of CuO formation, with CuO formation being much more prevalent in the 200 nm $MoSi_2$ sample. In fact, the copper layer is virtually all consumed for the 200 nm barrier. Small Cu_2O peaks were detected for many of the samples, but CuO was the predominant oxidation product. Additional small peaks coincide with hexagonal $MoSi_2$ and lower molybdenum silicide phases, Mo_5Si_3 and Mo_3Si (discussed in later sections).

Oxidation kinetics were quantified by taking thickness measurements of the oxide that had grown on the surface of the $MoSi_2$ layer. A minimum of 20 measurements, and as many as 50, were taken at random locations along the oxide. An average value was calculated along with the standard deviation. Cross-sections were made for either the SEM or TEM depending on the oxide thickness. Because SEM samples were quicker and easier to prepare, whenever possible the SEM was employed. The practical resolution limitation for these samples was an oxide thickness that was greater than ≈250 nm. Thicknesses smaller than this could not be resolved with confidence. Samples prepared for the SEM were subjected to the same initial preparation as the TEM, but dimpling and ion milling are not necessary.

TEM cross-section samples were subject to specimen preparation artefacts as a result of ion milling. The outer CuO layer was reduced to polycrystalline copper (Fig. 8, Table III). During the ion milling stage of specimen preparation, the sample is exposed to vacuum of close to 10^{-6} torr and a 4 kV Ar^+ ion beam. Order of magnitude calculations indicate that the Ar^+ beam could impart sufficient kinetic energy to

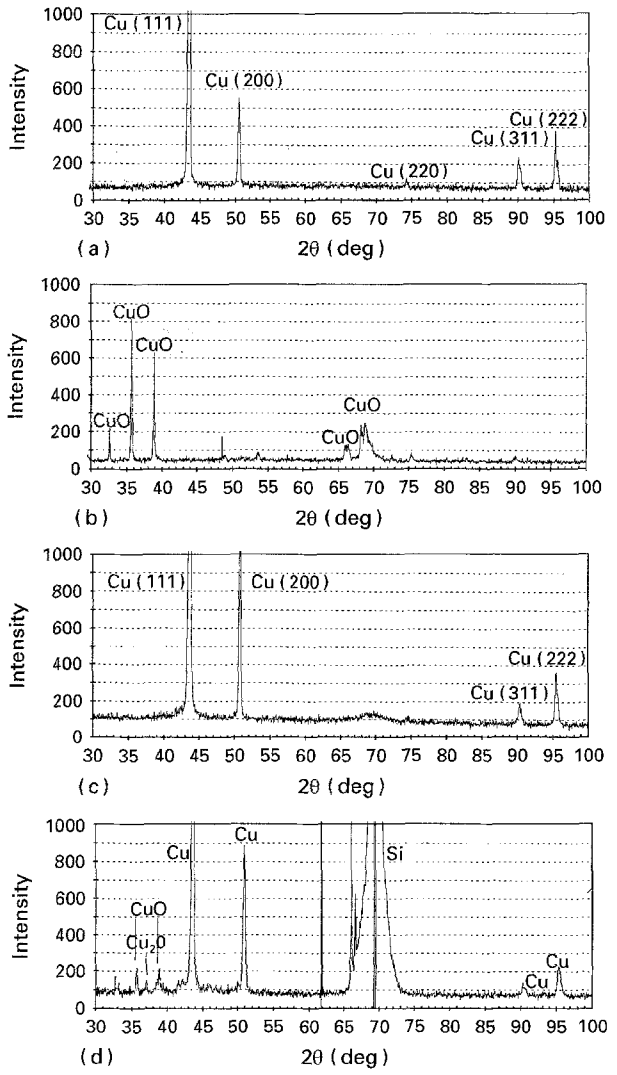

Figure 7 XRD spectra from (a, b) 200 nm and (c, d) 400 nm $MoSi_2$ barrier samples. (a, c) As-deposited; (b, d) 800 °C, 10 min.

reduce CuO to metallic copper. The reduction of CuO in a vacuum has been reported previously by Li and Mayer [37]. CuO heated to 550–680 °C in a vacuum of 2×10^{-7} torr at 550–680 °C was partially reduced to Cu_2O grains in a CuO matrix. The reduction rate was found to be faster in thin-film samples than bulk samples because of smaller grain sizes. The grain boundaries provide easy paths for oxygen out-diffusion resulting in lower phase transformation temperature in thin-film samples. CuO reduction in this work was minimized by reducing sputtering time and ion energy, as well as providing liquid-nitrogen cooling of the specimens. Oxide reduction was not a problem in SEM cross-sections, as they were not ion milled. This is reflected in the differences in the porosity between TEM and SEM samples; the CuO layer in the TEM sample is more porous (Fig. 8).

Cross-sections of samples annealed at 600, 700, 800 and 850 °C were prepared. All samples showed a trend of increasing oxide thickness with time for a given temperature, except for 200 nm barrier samples annealed at 850 °C – the oxide thickness varied from 3.4–3.7 μm. A representative SEM SE image of a 200 nm $MoSi_2$ sample annealed at 850 °C for 5 min is shown in Fig. 9. The underlying copper is missing in

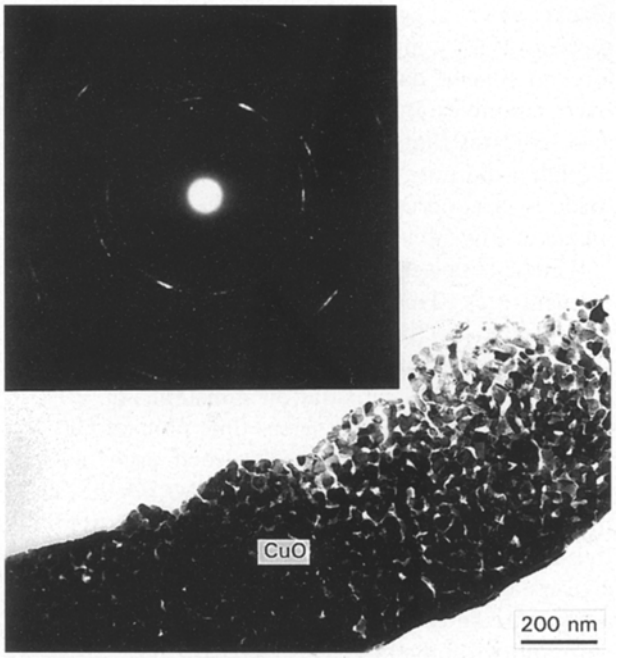

Figure 8 TEM bright-field image and SAD pattern of a cross-section of a 200 nm $MoSi_2$ sample annealed at 700 °C for 10 min, showing the oxide layer. The CuO layer has, in fact, been reduced to copper during specimen preparation. Most of the rings in the SAD pattern can be indexed as fcc copper, as shown in Table III. Crystallographic data were obtained from [25].

TABLE III The outer CuO layer reduced to polycrystalline copper

d (nm)	Relative intensity	*d* (nm) – *hkl*		
		Cu	Cu_2O	CuO
0.244	Weak		0.246–1 1 1	0.252–$\bar{1}$ 1 1
0.211	1	0.209–1 1 1	0.213–2 0 0	0.231–2 0 0
0.182	2	0.181–2 0 0		0.187–$\bar{2}$ 0 2
0.149	Weak		0.151–2 2 0	0.151–$\bar{1}$ 1 3
0.127	3	0.128–2 2 0	0.129–3 1 1	0.126–$\bar{2}$ 2 2
0.109	4	0.109–3 1 1		
0.086	5	0.093–4 0 0		
0.080	6	0.083–4 2 0		

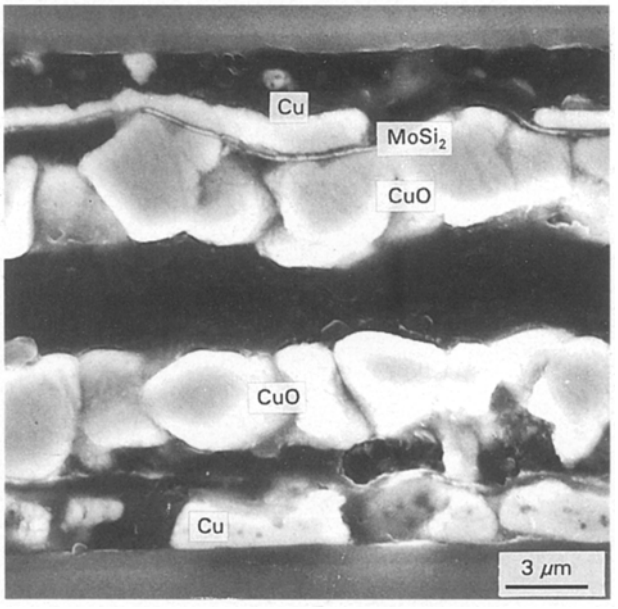

Figure 9 SEM SE image of a 200 nm $MoSi_2$ barrier sample annealed at 850 °C for 5 min.

places which suggests the oxide thickness stopped growing as the copper became depleted locally. Therefore no kinetic data were obtained for the 200 nm barrier samples annealed at 850 °C. The same figure also indicates that $MoSi_2$ remained continuous even though it did not remain planar. The grain size of the oxide is in good agreement with the plan-view SEM image of Fig. 5d.

Kinetic data were calculated for the remaining three temperatures. Thickness measurements were taken and plotted as thickness squared versus time. The slope of the best-fit straight line for the parabolic plot gives the parabolic oxidation constant, k_p. Fig. 10 shows thickness squared verses time plots at 600, 700 and 800 °C. The error bars for each point are indicated; otherwise they are contained within the size of the data marker. The x intercept, which is essentially the incubation time for initial oxide formation, decreases as the temperature increases. Fig. 11 shows a comparison of the kinetic data for copper samples with and without the $MoSi_2$ barrier.

The oxide that formed on the surface of the coated samples was virtually all CuO, compared with bare copper which was almost entirely Cu_2O. Because the oxide that forms is different, a more appropriate way of comparing the oxidation kinetics is to calculate the amount of copper consumed. The parabolic rate constants, activation energy, the oxide thickness for 15 min anneals and the amount of copper consumed

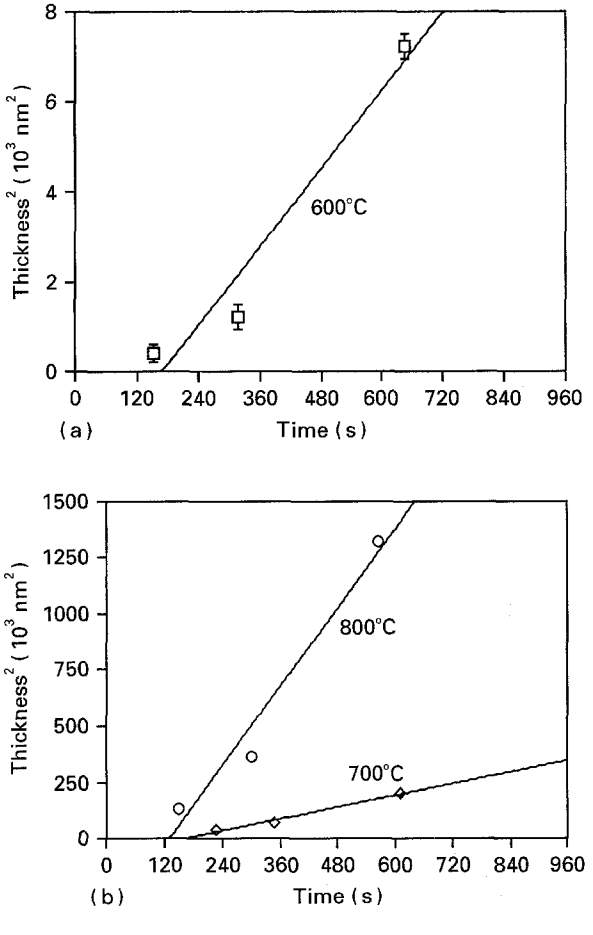

Figure 10 (a, b) Kinetic plots for the 200 nm $MoSi_2$ barrier samples.

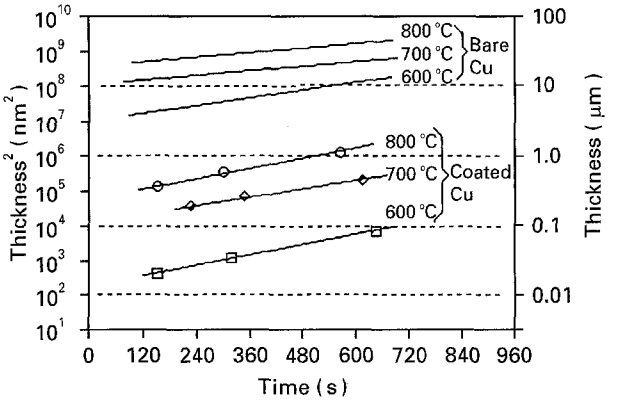

Figure 11 Plot of kinetic data from bare copper samples and 200 nm $MoSi_2$ barrier samples.

are tabulated for the 200 nm barrier samples and for bare copper in Table IV. Because the densities of the two oxides differ by only 0.4 g cm^{-3} there is not much difference when comparing the oxidation behaviour of bare copper with coated copper, either in terms of oxide thickness or by the amount of copper consumed. The copper consumed is reduced by ≈143 times at 600 °C, ≈50 times at 700 °C, and ≈33 times at 800 °C for a 200 nm $MoSi_2$ diffusion barrier compared with bare copper.

Kinetic data for the 400 nm barrier samples were calculated for 600, 700, 800 and 850 °C. Parabolic rate constants, k_p, were obtained from the data plotted in Fig. 12. Error bars for each point are indicated; otherwise they are contained within the size of the data marker. At 600 °C, only 15 and 10 min data points are shown; there was no surface oxide below 10 min. Once again, incubation times increased as the temperature decreased. Fig. 13 shows a comparison of the 400 nm barrier data with the data for bare copper. There is a significant improvement for the 400 nm $MoSi_2$ barrier samples, even at 850 °C. The data for the rate constants, oxide thickness at 15 min, and copper consumed at 15 min, for bare copper and the 400 nm barrier samples are tabulated in Table III. The values in brackets indicate the improvement over bare copper. At 850 °C there is a 200 times improvement over the amount of copper consumed to bare copper. This corresponds to a CuO layer ≈300 nm thick at 15 min.

Fig. 14 shows Arrhenius plots of the kinetic data from Fig. 12 (400 nm $MoSi_2$) and Fig. 10 (200 nm $MoSi_2$). The 200 nm data fit a straight line reasonably well, yielding an apparent activation energy of 215 kJ mol^{-1} (compared with 84 kJ mol^{-1} for bare copper). The 400 nm barrier data are less straightforward. Two curves (a and b in Fig. 14) could be drawn, suggesting a change in the diffusion mechanism of copper through the barrier layer at about 700 °C. If the two points for 600 and 700 °C (curve a) are joined to form a straight line then the apparent activation energy is 220 kJ mol^{-1}, which is close to the 215 kJ mol^{-1} for the 200 nm $MoSi_2$ samples. This result is not surprising, because a thicker $MoSi_2$ diffusion barrier should shift the previous plot for 200 nm $MoSi_2$ coating upwards, without a change in slope (providing the oxidation process is the same for both).

TABLE IV Kinetic data for bare copper and diffusion barrier samples[a]

		600 °C	700 °C	800 °C	850 °C
k_p ($cm^2 s^{-1}$)	200 nm $MoSi_2$	1.45×10^{-13} (15 800 ×)	4.37×10^{-12} (1580 ×)	2.95×10^{-11} (710 ×)	
	400 nm $MoSi_2$	3.57×10^{-14} (64 400 ×)	7.65×10^{-13} (9050 ×)	9.30×10^{-13} (22 580 ×)	1.09×10^{-12} (26 150 ×)
	Bare Cu	2.30×10^{-9}	6.92×10^{-9}	2.10×10^{-8}	2.85×10^{-8}
Oxide thickness at 15 min (nm)	200 nm $MoSi_2$	103 (137 ×)	570 (46 ×)	1500 (31 ×)	
	400 nm $MoSi_2$	34 (415 ×)	238 (111 ×)	270 (176 ×)	293 (191 ×)
	Bare Cu	14 100	26 500	46 900	56 000
Cu consumed at 15 min (nm)	200 nm $MoSi_2$	60 (143 ×)	330 (50 ×)	870 (33 ×)	
	400 nm $MoSi_2$	20 (430 ×)	138 (117 ×)	157 (182 ×)	170 (200 ×)
	Bare Cu	8600	16 160	28 600	34 150
Apparent activation energy (kJ mol^{-1})	200 nm $MoSi_2$		215		
	400 nm $MoSi_2$	(a) 220 (b) 22	(c) 110		
	Bare Cu		83.6		

[a] Numbers in parenthesis indicate the improvement over bare copper.

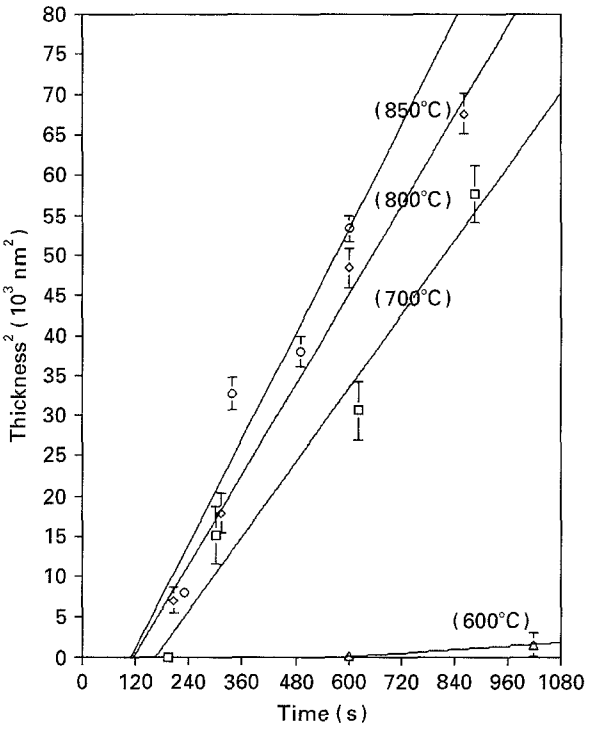

Figure 12 Kinetic plots for the 400 nm $MoSi_2$ barrier samples.

Joining the other three data points (curve b) gives an apparent activation of 22 kJ mol^{-1}. The parabolic rate constants above 700 °C are within an order of magnitude of each other, resulting in the shallow slope given by curve b. Another way to interpret the data is through c (Fig. 14), where all the data points are fitted to a single curve. The apparent activation energy in this case is 110 kJ mol^{-1}, although the fit is not particularly good. A single line through the data points suggests the same oxidation mechanism for copper for all the temperatures of interest. To determine confidently if there is a change in the diffusion mechanism, more data points are needed.

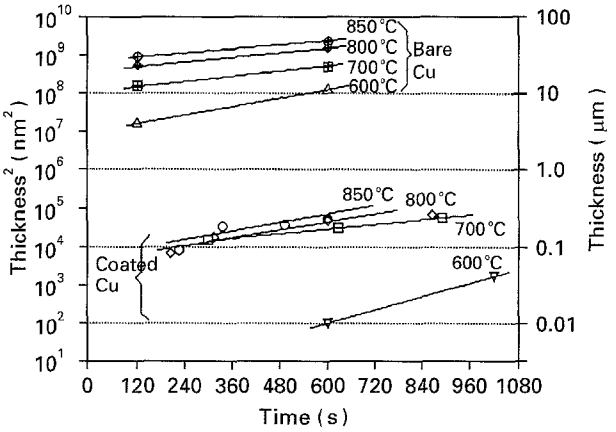

Figure 13 Plot of kinetic data from bare copper samples and 200 nm $MoSi_2$ barrier samples.

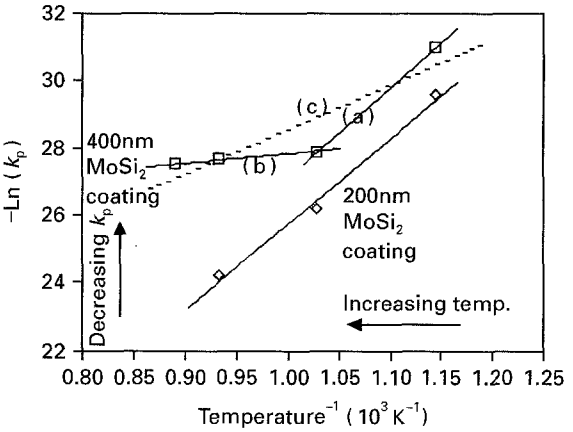

Figure 14 Arrhenius plots of parabolic rate constants from 200 and 400 nm $MoSi_2$ barrier kinetic data.

The $MoSi_2$ barrier was examined, primarily by TEM, in an effort to understand better its role in preventing copper oxidation and to understand differences in the behaviour of the 200 and 400 nm barriers. For both barrier thicknesses, the as-deposited

structure was amorphous. Annealing resulted in two significant changes, i.e. loss of silicon from the barrier layer (and the corresponding dissolution of copper in the barrier layer) and crystallization of the amorphous layer. Loss of silicon was a consequence of the relatively high solid solubility of silicon in copper, which reaches a maximum of ≈ 12 at%. Silicon dissolution in copper, from a practical stand point, is undesirable because at the very least it would lead to an increase in the resistivity of the copper. The silicon concentration in the copper layer was fairly uniform although lower than the solubility limit. Because the amount of copper is fixed (≈ 2 μm) for both barrier thicknesses, silicon loss was more pronounced for the 200 nm barrier samples. An EDX spectrum of the copper layer near the $MoSi_2$/Cu interface, for the 400 nm barrier sample annealed at 800 °C for 2 min, is shown in Fig. 15. Also shown are EDX spectra, from the same sample, of the CuO layer and the diffusion barrier. Note, the absence of oxygen in CuO (already discussed) and the presence of a significant amount of copper in the barrier layer. Partial crystallization of $MoSi_2$ was apparent for the lowest annealing temperatures (600 °C). However, the crystalline product or products were dependent on the amount of silicon loss. The amorphous layer transformed to $MoSi_2$ (hexagonal metastable form) and Mo_5Si_3 for the 400 nm barrier samples and Mo_5Si_3 and Mo_3Si for the 200 nm samples. Phase identification was accomplished through a combination of semiquantitative EDX and electron diffraction analysis in the TEM and corroborated by XRD. Fig. 16 shows a comparison between the 400 nm $MoSi_2$ barrier samples annealed at 600 °C for 2 min, and 850 °C for 10 min. The patterns are indexed in Table V. Dark-field images and SAD patterns, from plan-view specimens, are also shown for both temperatures. For the 600 °C anneal, the SAD pattern has a diffuse ring in addition to the other sharper rings, indicating that the $MoSi_2$ layer is still partially amorphous. The strongest diffraction rings correspond to hexagonal $MoSi_2$, while a few of the weaker rings correspond to Mo_5Si_3. At 850 °C, the diffuse ring is gone and the diffraction rings are not as continuous. The loss in ring continuity is due to grain growth – the grain size has increased from < 20 nm at 600 °C to ≈ 60 nm at 850 °C. It is expected that an increase in grain size would be beneficial to the diffusion barrier properties because there are fewer short-circuit paths for copper diffusion. The relative decrease in grain-boundary area, from 600–850 °C, is about three-fold. For the 200 nm barrier samples, the grain size at 600 °C was < 10 nm and increased to about > 40 nm at 850 °C.

The phase transformations and grain growth, during annealing, may account for the differences in trends for the two different $MoSi_2$ barrier layers. One interpretation of the apparent activation energy plot in Fig. 14 suggests a change in the diffusion mechanism for the 400 nm $MoSi_2$ barrier. Also, grain growth at higher temperatures reduces the number of short-circuit paths for copper transport, which would slow the diffusion rate. The excessive loss of silicon for the 200 nm $MoSi_2$ barrier may reduce the thinner

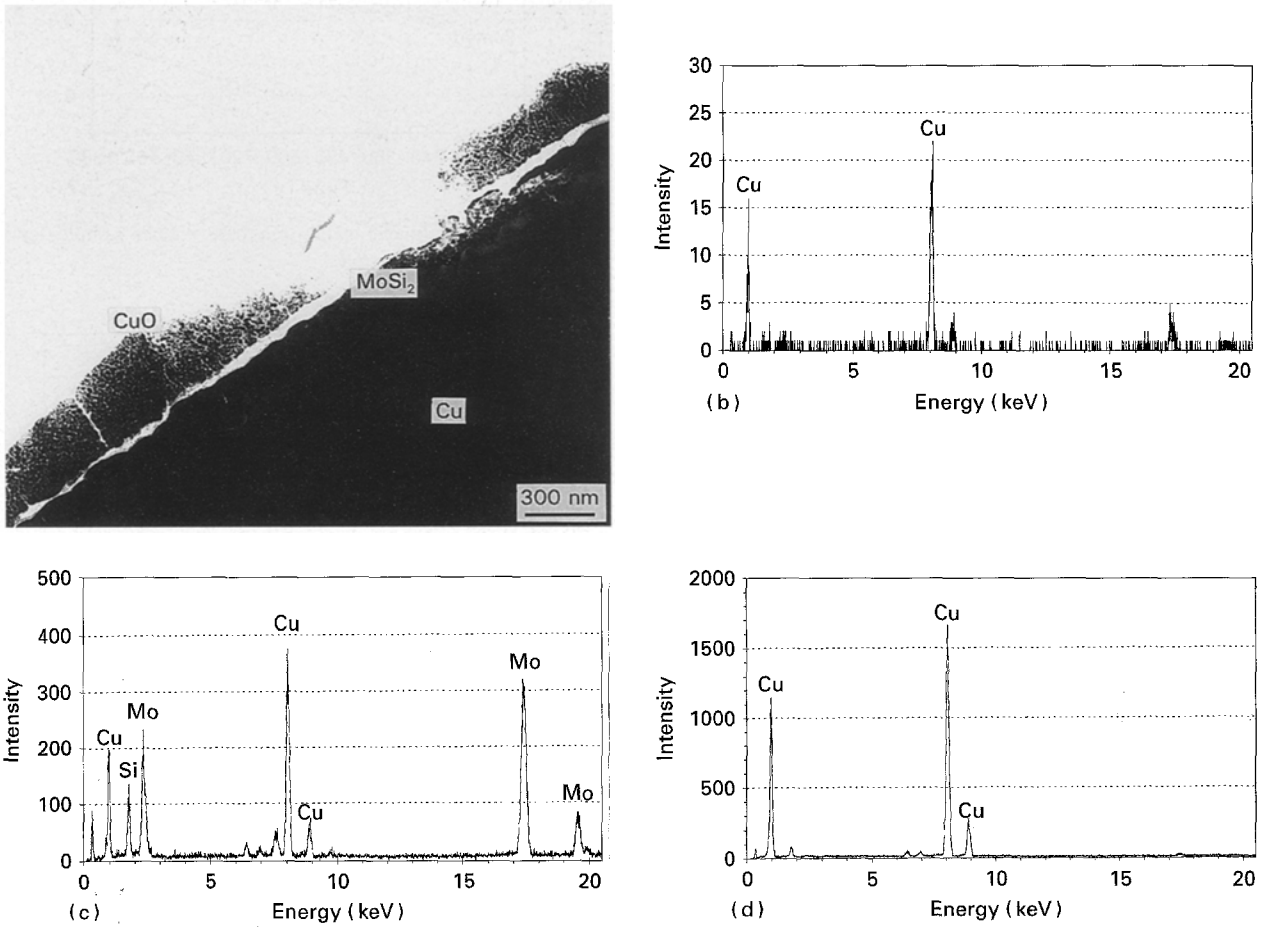

Figure 15 (a) TEM bright-field image and (b–d) EDX spectra from 200 nm $MoSi_2$ barrier sample annealed at 800 °C for 2 min. (b) CuO, (c) $MoSi_2$ and (d) Cu.

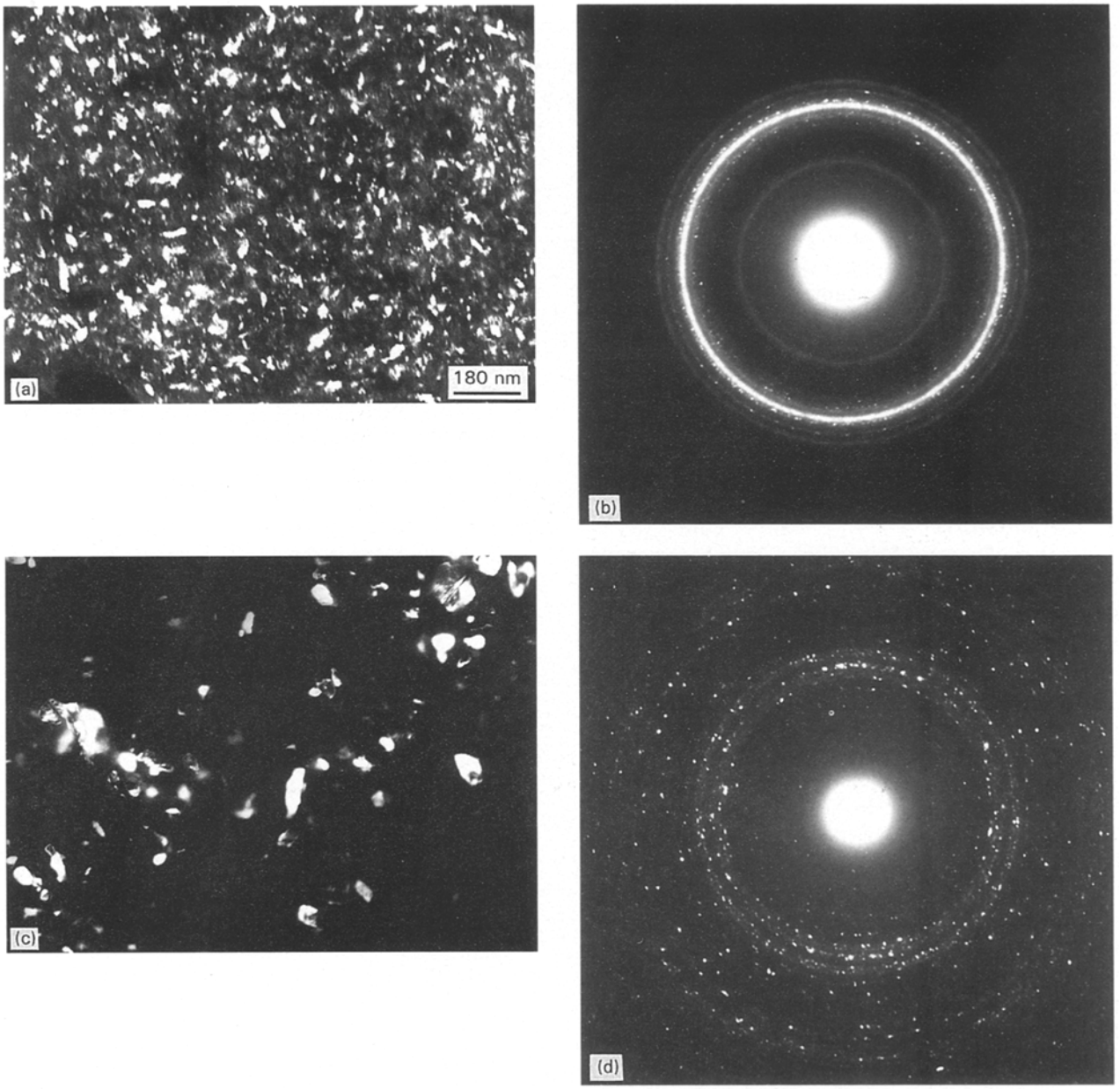

Figure 16 TEM dark-field images and SAD patterns from plan view specimens of 400 nm $MoSi_2$ barrier samples annealed at (a, b) 600 °C for 2 min and (c, d) 850 °C for 10 min. The patterns are indexed in Table V. Crystallographic data were obtained from [25].

TABLE V

		Mo_5Si_3 (tetragonal)			$MoSi_2$ (hexagonal)		
d (nm)	Intensity	*d* (nm)	*hkl*	Intensity	*d* (nm)	*hkl*	Intensity
0.394	Medium				0.398	100	10
0.344	Medium				0.337	101	50
0.327	Weak	0.324	211	25			
0.302	Weak	0.305	310	21			
0.245	Medium	0.245	002	25			
0.218	1	0.219	202	38	0.217	111	100
0.212	2	0.211	411	100			
0.200	3				0.200	200	16
0.188	4				0.188	112	40
0.147	Weak				0.147	211	20
0.134	Weak	0.134	413	33	0.133	114	16

barrier's effectiveness as the temperature increases. The grain size of the 200 nm $MoSi_2$ did not increase as much as the 400 nm barrier which also accounts for its poorer performance at high temperatures. Significant amounts of copper are present in the $MoSi_2$ layer (for both barrier thicknesses). Copper is probably present in the grain boundaries of the $MoSi_2$ layer, as it diffuses to the surface to form copper oxide, and

copper may also be dissolved in the lattice. Whatever the case, the presence of copper may affect the temperatures at which phase transformations occur in $MoSi_2$. Further analysis of the presence of copper in $MoSi_2$ would be needed to make any confident conclusions.

Although the details of copper diffusion through $MoSi_2$ are far from understood, the results are generally favourable. At 600 °C for 15 min, for a 400 nm $MoSi_2$ layer sputter deposited on to copper, ≈20 nm of copper is consumed to form CuO, compared with 8.6 μm of copper consumed for bare copper. At 850 °C for a 400 nm $MoSi_2$ layer sputter deposited on to copper, only ≈170 nm of copper is consumed, compared with ≈34 μm of copper for bare copper.

4. Conclusions

A number of conclusions can be drawn based on the work done on the oxidation behaviour of copper covered with a $MoSi_2$ diffusion barrier, either 200 or 400 nm thick.

1. $MoSi_2$, electron deposited on to copper, is initially amorphous. Annealing results in crystallization and silicon loss to the underlying copper. For the 200 nm barrier, loss of silicon leads to the formation of Mo_3Si and Mo_5Si_3. In the 400 nm barrier samples, hexagonal $MoSi_2$ and Mo_5Si_3 form.

2. $MoSi_2$ diffusion barriers significantly reduce copper oxidation for the temperature range studied (600–850 °C). The amount of copper consumed by oxidation, for a 200 nm $MoSi_2$ barrier relative to bare copper, was reduced by ≈140 times at 600 °C, and ≈30 times at 800 °C. For 400 nm of $MoSi_2$, the improvement is ≈430 times at 600 °C and ≈200 times at 850 °C.

Acknowledgement

The authors thank the Alberta Microelectronic Centre for providing access to deposition facilities.

References

1. D. E. PITKANEN, J. P. CUMMINGS and C. J. SPEERSCHNEIDER, *Solid State Technol.* October **23** (1980) 141.
2. J. R. LARRY, R. M. ROSENBERG and R. O. UHLER, *IEEE Trans. Compon. Hybrids Manuf. Technol.* CHMT-3 (2) (1980) 211.
3. J. LI, Y. SHACHAN-DIAMAND and J. W. MAYER, *Mater. Sci. Rep.* **9** (1992) 1.
4. J. M. E. HARPER, E. G. COLGAN, C-K. HU, J. P. HUMMEL, L. P. BUCHWALTER and C. E. UZOH, *MRS Bull.* **18** (8) (1994) 23.
5. S-Q. WANG, *ibid.* **18** (8) (1994) 30.
6. M. A. NICOLET, *Thin Solid Films* **52** (1978) 415.
7. R. PRETORIUS, *J. Electrochem. Soc.* **128** (1981) 107.
8. R. PRETORIUS, W. STRYDOM, J.W. MAYER and C. COMRIE, *Phys. Rev.* **B22** (1980) 1885.
9. M. BARTUR and M. A. NICOLET, *Appl. Phys. Lett.* **40** (1982) 175.
10. J. R. CHEN, Y. C. LIU and S. D. CHU, *ibid.* **40** (1982) 263.
11. S. P. MURARKA and C. CHANG, *ibid.* **37** (1980) 639.
12. S. P. MURARKA, D. B. FRASER, W. S. LINDENBERGER and A. K. SINHA, *J. Appl. Phys.* **51** (1980) 3241.
13. T. MOCHIZUKI and M. KASHIWAGI, *J. Electrochem. Soc.* **127** (1980) 1128.
14. T. INOUE and K. KOIKE, *Appl. Phys. Lett.* **33** (1978) 826.
15. B. L. CROWDER and S. ZIRINSKY, *IEEE J. Solid State Circ.* **SC-14** (1979) 291.
16. A. K. SINHA, *J. Vac. Sci. Technol.* **19** (1981) 778.
17. D. R. WOLTERS, *J. Electrochem. Soc.* **127** (1980) 2073.
18. P. T. B. SHAFFER, "Plenum Press Handbook of High Temperature Materials No. 1 Materials Index" (Plenum Press, New York, 1964).
19. M. A. NICOLET and S. S. LAU, in "VLSI Electronics: Microstructural Science", edited by N. G. Einsprach Vol. 7 (Academic Press, San Diego, 1983) Ch. 6.
20. E. A. BRANDES, "Smithells Metals Reference Book", 6th Edn. (Butterworths, London, 1983).
21. E. I. ALLESSANDRINI, D. R. CAMPBELL and K. N. TU, *J. Appl. Phys.* **45** (1974) 4888.
22. VON E. FITZER, in "Plansee Proceedings, 2nd Seminar" edited by F. Benesovsky, Reutte/Tyrol (1956) 56.
23. T. C. CHOU and T. G. NIEH, *J. Mater Res.* **8** (1993) 214.
24. *Idem, J. Metals* December (1993) 15.
25. Powder Diffraction Files, JCPDS-International Center for Diffraction Data (1993).
26. J. J. PETROVIC, *MRS Bull.* **18**(7) (1993) 35.
27. V. ANANTH, S. K. BOSE and S. C. SIRKAR, *Scripta Metall.* **14** (1980) 687.
28. C. ZHOU and W. W. SMELTZER, *High Temp. Oxid. Sulph. Proc.* **22** (1990) 43.
29. C. WAGNER, *Phys. Chem.* **21** (1993) 25.
30. *Idem.* "Handbuch der Metallphysik", edited by G. Masing 1, Part 2 (Akademische verlagsgesellschaft, Leipzig, 1940) p. 144.
31. G. VALENSI, in "Pittsburgh International Conference on Surface Reactions" (Corrosion, Pittsburgh, 1948) p. 156.
32. A. RONNQUIST and H. FISCHMEISTER, *J. Inst. Metals* **89** (1990–61) 65.
33. M. MATYAS, *Czech. J. Phys.* **5** (1955) 214.
34. E. A. GULBRANSEN and W. R. McMILLAN. *J. Electrochem. Soc.* **99** (1952) 393.
35. G. GARNAUD, *Oxid. Metals* **11** (3) (1977) 127.
36. D. W. BRIDGES, J. P. BAUR, G. S. BAUR and W. M. FASSELL, *J. Electrochem. Soc.* **104** (1957) 749.
37. J. LI and J. W. MAYER, *Mater. Chem. Phys.* **32** (1992) 1.

Received 27 January
and accepted 22 March 1995